PROCEEDINGS OF SPIE

Low loss TiO2 channel waveguides

Hegeman, I., Dijkstra, M., García-Blanco, S.

SPIE.

Low loss TiO$_2$ channel waveguides

I. Hegeman[1], M. Dijkstra[1], S.M. García-Blanco[1]

[1]Optical Sciences Group, MESA + Institute for Nanotechnology,
University of Twente, P.O. Box 217, 7500 AE Enschede, The Netherlands

ABSTRACT

TiO$_2$ is gaining interest as material for integrated photonics, due to its high refractive index, large transparency window and high non-linear refractive index. Its low phonon energy makes it attractive for the realization of active devices in the visible frequency range. In this work, we optimize different process steps of the fabrication of low loss TiO$_2$ channel waveguides. The TiO$_2$ layers are deposited by DC sputter deposition, using a mixed Ar/O$_2$ plasma. Removing the hysteresis in the deposition process, results in reduced propagation losses of the TiO$_2$ films (estimated less than 1.5 dB/cm at 632 nm wavelength). An E-beam lithography process is utilized to reduce the sidewall roughness of the waveguides. Different reactive gasses are compared to optimize the reactive ion etching recipe. BCl$_3$ in combination with HBr shows to be most beneficial for etching TiO$_2$ with high selectivity towards negative E-beam resist. A selectivity of 2.7 for TiO$_2$ over the E-beam resist is obtained. The performance of a TiO$_2$ a channel waveguide fabricated with the process before and after optimization is compared. The waveguide fabricated using the non-optimized process exhibited losses of 7.82±0.52 dB/cm at a wavelength of 632.8 nm, after applying an SiO$_2$ cladding. After process optimization, 5.08±0.65 dB/cm were obtained, without an SiO$_2$ cladding.

Keywords: TiO$_2$, channel waveguide, Sputter deposition, hysteresis, UV contact lithography, E-beam lithography, reactive ion etching, propagation losses.

INTRODUCTION

TiO$_2$ possesses a high refractive index of 2.3-2.4 [1,2] and a large transparency window from the visible to infrared wavelength range due to its high bandgap of 3 eV [3]. These material properties make TiO$_2$ promising for integrated photonic circuits with a small footprint. The possibility to dope TiO$_2$ with, for example, rare earth ions or Si [4–7] makes TiO$_2$ promising for active on chip devices. TiO$_2$ exhibits a high non-linear refractive index, resulting in the demonstration of third harmonic generation [8], supercontinuum generation [9], spectral broadening [10] and four-wave mixing [11]. The negative thermo-optic coefficient [12] allows for the realization of athermal devices [13], by combining TiO$_2$ with, for example, Si$_3$N$_4$ [14,15] or silicon [16,17]. The high refractive index has allowed the demonstration of high efficiency in waveguide enhanced Raman spectroscopy [18,19].

Low propagation losses need, however, to be achieved in order for TiO$_2$ waveguides to find real applications. Current results in literature report channel waveguide losses down to 9.7 dB/cm at a 632.8 nm [1] and 4 dB/cm at 1550 nm [2], using conventional fabrication techniques, i.e. deposition, lithography and etching. A lift-off process has shown losses as low as 7.5 dB/cm at 632.8 nm and 1.2 dB/cm at 1550 nm [20].

TiO$_2$ is commonly deposited by reactive sputter deposition [1,2,11,21–23]. The structure of the deposited film is very dependent on the oxygen partial pressure during the process. Unfortunately, hysteresis in the process prevents in many cases to reach the optimum deposition parameters. In this work we experimentally demonstrate the influence of the total gas flow and target size during the sputtering process, as predicted by the Berg model [24]. A method is shown to optimize the sputter deposition process for low-loss films.

The etching of TiO$_2$ waveguides is usually performed using reactive ion etching with fluoride containing gasses [1,2,11,25], often combined with Ar or O$_2$. Furthermore, these studies report the use of a Cr of Al hard mask, made by E-beam lithography using positive resist followed by lift-off. The use of negative E-beam resist can result in a much simpler process. However, this requires high etch selectivity of TiO$_2$ towards resist. Studies have been performed on the properties of different reactive gasses, such as CF$_4$ [26–28], SF$_6$ [28,29], Cl$_2$ [29,30] and BCl$_3$ [31]. In this work, we compare systematically the influence of SF$_6$, CHF$_3$, HBr, BCl$_3$ and Cl$_2$ as reactive gas and optimize the etching recipe.

PROCESS OPTIMIZATION

The fabrication of TiO$_2$ is performed in three process steps. First a TiO$_2$ layer is deposited by means of reactive sputter deposition. The deposition is followed by a lithography and etching step. Each of the three fabrication steps is optimized in order to reduce the propagation losses of the resulting TiO$_2$ channel waveguide.

Sputter deposition

Thin TiO_2 films are deposited by means of DC reactive sputter deposition from a 4 inch 99.999% pure Ti target in the TCOater in the MESA+ cleanroom. The deposition was performed at a constant pressure of $6 \cdot 10^{-3}$ mbar, a target to substrate distance of 176 mm, a constant DC power of 500 W and a temperature of the substrate between 20-30 °C. A Si wafer with an 8 μm thick layer of thermal SiO_2 is used as substrate. The optimum oxygen flow is determined by studying the bias curve, which shows the voltage between the target and ground, depending on the oxygen flow into the reactor.

As the oxygen flow increases, the target gets more oxidized. For TiO_2 the secondary electron yield is lower than for Ti [32]. When applying a constant power to the target, the current drops and, consequently, the bias voltage increases, as the target oxidizes. The bias curve is related to the oxidation state of the target. The measurement of the bias curve starts at an O_2 flow of 0 sccm, which is then increased. After reaching the top of the bias curve, the same curve is measured for decreasing O_2 flow. It is experimentally observed that depositions at the left (low O_2 flow) side of the curve result in non-stoichiometric layers, which show no optical guiding. Depositions performed at the right side of the curve show stoichiometric optically guiding layers. However, the morphology depends on the O_2 flow. The best optically guiding layers are deposited in the region of optically guiding layers, but with as low O_2 flow as possible [33]
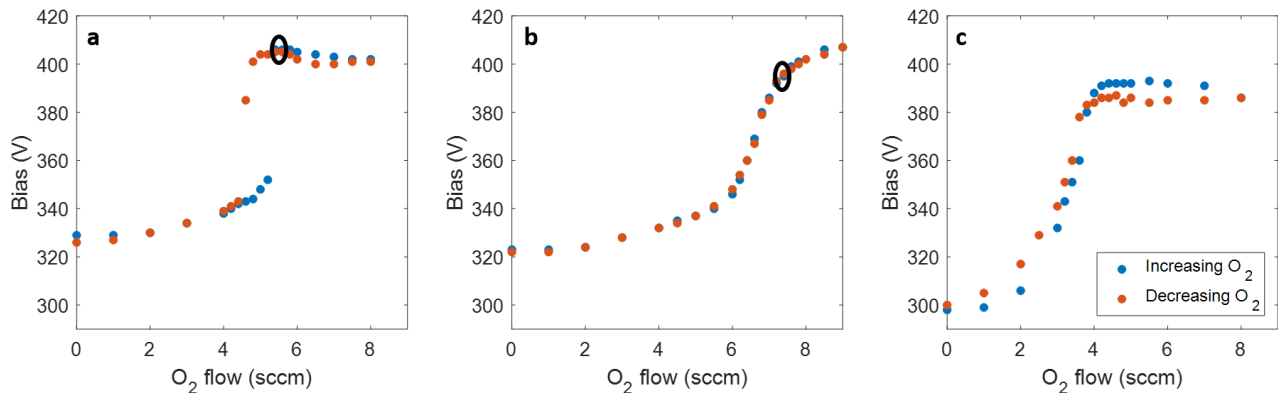
Figure 1. Bias curve for (a) 40 sccm Ar flow and a 4" Ti target, (b) 80 sccm Ar flow and a 4" Ti target and (c) 40 sccm Ar flow and a 2" Ti target.

The measured bias curves are shown in figure 1. In case of figure 1a, a 4" Ti target and a constant Ar flow of 40 sccm are used and hysteresis is observed in the bias curve. Any deposition performed in the hysteresis part of the curve, in this case between 4.4 and 5.4 sccm of O_2 flow, will not be stable. In this case the best optical layers are obtained at point indicated with the black ellipse, which corresponds to an O_2 flow of 5.6 sccm. Propagation of the resulting slab mode is shown in figure 2a, which does show reasonable optical guiding, but significant propagation losses. In order to perform depositions at lower a point closer to the metallic regime, the hysteresis needs to be taken out of the process. This can be done by increasing the Ar flow into the reactor or by reducing the target size [34]. This is shown in figure 1b for an Ar flow of 80 sccm with a 4" Ti target and in figure 1c for an Ar flow of 40 sccm with a 2" Ti target. The case of a higher Ar flow with the bigger target is used to deposit a second layer, since this case will give a higher deposition rate compared to the case of a 2" target. Figure 2b shows the propagation of a slab mode at a wavelength of 632.8 nm, through a TiO_2 layer deposited with 80 sccm Ar and 7.3 sccm O_2 flow, which corresponds to the marked point in figure 1b. It is observed that the propagation losses are significantly lower, compared to the layer shown in figure 2a.
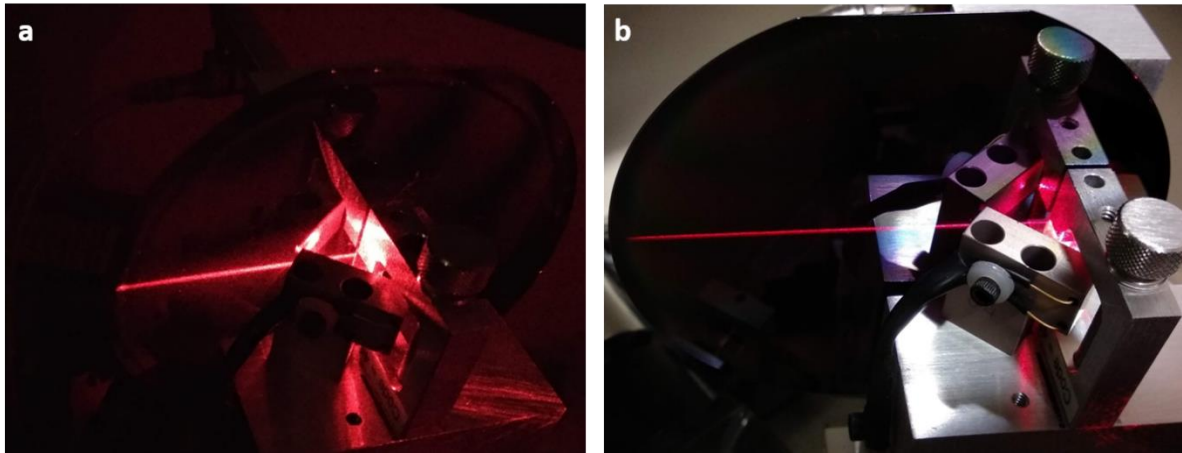
Figure 2. Propagation of slab modes at a wavelength of 632.8 nm in TiO$_2$ layers. For both images the coupling point is located at the right side of the image and the mode propagates to the left. (a) Propagation through a TiO$_2$ layer deposited with 40 sccm Ar and 5.6 sccm O$_2$. (b) Propagation through a TiO$_2$ deposited with 80 sccm Ar and 7.3 sccm O$_2$.

The origin of the hysteresis can be explained using the Berg model [24]. Figure 3a shows the reactive gas pressure in the reactor as a function of the reactive gas (O$_2$) flow into the chamber. It must be noted that these figures are reproduced based on the Berg model and do not match with the bias curves shown in figure 1. They do however help in qualitative understanding of the process. Figure 3a shows 3 different possible reactive gas pressures for a single value of the reactive gas flow, for reactive gas flows between approximately 1.8 and 2.9 sccm of reactive gas flow. As a result, there are three different compound fractions possible of both the target and the deposited layer for these values of reactive gas flow, shown in figure 3b. As explained before, the compound fraction is related to the secondary electron yield and thereby the obtained current and voltage at a certain power. When the reactive gas flow is increased, the compound fraction of the target increases gradually, until about 2.9 sccm. When further increasing the reactive gas flow, a jump in the compound fraction is observed, following the black dotted line. When decreasing the reactive gas flow again, a jump occurs at lower reactive gas flow. The process configuration in between the two black lines cannot be obtained, without removing the hysteresis.
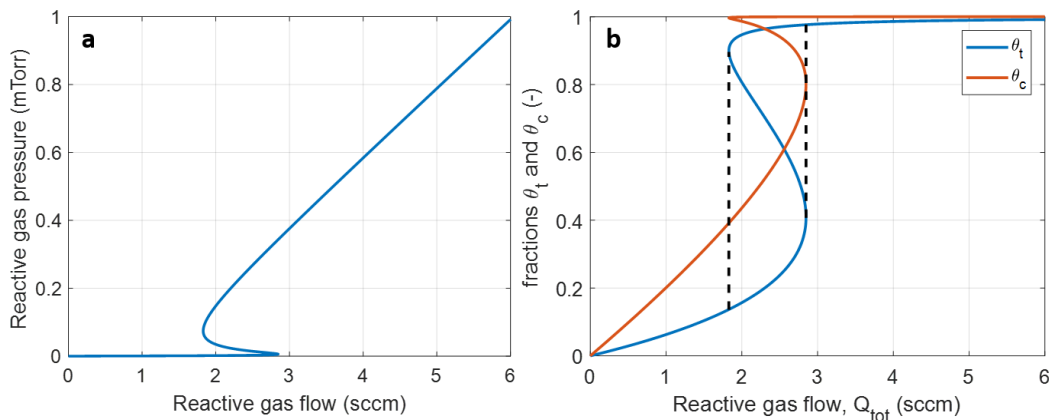
Figure 3. (a) reactive gas pressure vs reactive gas flow and (b) the compound fraction at both the wafer (θ_c) and the target (θ_t), both reproduced from the Berg model [24].

The hysteresis is caused by gettering of the reactive gas at the collection area (i.e. the wafer). When starting at a reactive gas pressure of zero and increasing the reactive gas pressure, the amount of reactive gas consumption by the collection area increases rapidly due to the increased availability of the reactive gas, as shown by the yellow line in figure 4. However, the target gets oxidized, causing the sputter yield to drop, which causes a lower deposition rate. As a result the reactive gas consumption at the collection area decreases again. When this effect is bigger than the reactive gas

consumption of the target or the pump, hysteresis will be observed, since at a single reactive gas flow, there are multiple solutions for the reactive gas pressure. As shown in figure 1b, the hysteresis can be taken out of the process by increasing the gas flow (both Ar and O_2). Since for the actual deposition we work with a constant pressure, an increased gas flow will result in an increased flow towards the pump. When the slope of the pump line (figure 4a) is higher than the maximum negative slope of the collection area, no hysteresis will occur. Another possibility is reducing the target size, as is used in figure 1c. Reducing the target size reduces the deposition rate and thereby the getter effect of the collection area, which by the same reasoning takes out the hysteresis. Both methods for reducing the hysteresis in the reactive sputtering process were both predicted by the Berg model [34].
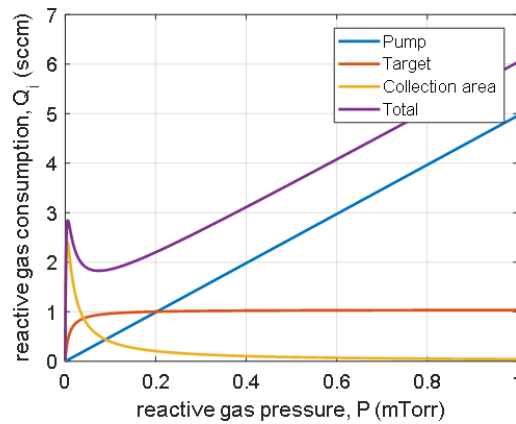
Figure 4. reactive gas consumption by the pump, target and collection area for varying reactive gas pressure, reproduced from the Berg model [24].

E-beam lithography

An origin of propagation losses in waveguide is the sidewall roughness. During the lithography process, roughness can occur in the resist patterns. When etching the structures, the roughness in the resist can be transferred to the waveguide structures. In order to reduce the sidewall roughness, high resolution resist patterns are required. An E-beam lithography (EBL) recipe is developed for negative resist (AR-N 7520.18). After dehydration of the substrate, an HMDS layer is spun at 4000 rpm for 45 s, to promote adhesion to the substrate. The resist is spun at 1500 rpm for 180 s, to get a homogeneous resist layer of 650-700 nm thick, followed by a baking step at 80 °C for 1 minute. A conductive coating (AR-PC 5091) is spun on top of the resist at 2000 rpm for 45 s, followed by a baking step at 50 °C for 2 minutes. The conductive coating is to prevent charging during the EBL process. Exposure is performed with the Raith EBPG 5150 in the MESA+ cleanroom, with a beam current of 80 nA, an acceleration voltage of 100 kV and a dose of 800 μC/cm^2. Development is performed in AR 300-47 developer for 60 s.
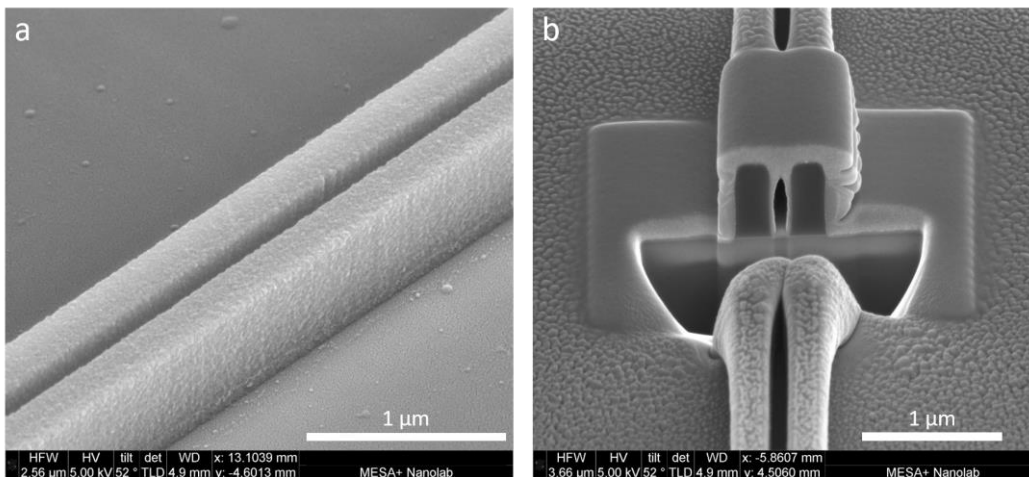
Figure 5. (a) Sideview of negative EBL patterns. (b) Cross-section of negative EBL patterns covered with a thin Pt layer to prevent rounding during the FIB milling process.

Figure 5a shows a sideview of a typical resist pattern. The observe roughness is partially caused by the applied SEM coating, which is required to prevent charging during imaging. To observe the gap of the structure, a cross-section is made by using a focused ion beam (FIB), as is shown in figure 5b. Prior to the FIB milling a Pt coating is deposited, to prevent rounding of the structure due to the FIB milling. The patterns show low amounts of roughness and structures with a width down to 300 nm and gaps down to 150 nm can be obtained.

Reactive ion etching

In order to obtain waveguide structures with straight sidewalls, a reactive ion etching recipe has been developed to etch TiO_2 with high selectivity towards photoresist. Before optimizing the etching recipe, the different available chemistries are compared. The etching is performed with the Plasma Pro 100 Cobra in the MESA+ cleanroom. The general process settings are summarized in table 1.

Pressure (mTorr)	Time (mm:ss)	HF power (W)	ICP power (W)	Temperature (°C)
10	01:00	20	1500	10

Table 1. Etch parameters

The etch rate of the negative EBL resist, the SiO_2 substrate and the TiO_2 film are compared for etching in SF_6, CHF_3 HBr, Cl_2 and BCl_3, which are the available gasses in the used etching machine. As shown in table 2, SF_6 shows the highest etching rate of TiO_2, however poor selectivity towards both resist and SiO_2. CHF_3 etches much slower, but with slightly better selectivity towards the resist. HBr and Cl_2 show hardly any etching of the TiO_2 layer. BCl_3 gives a relatively high etch rate, and a electivity higher than 1 towards the resist and 3 towards the SiO_2, which makes BCl_3 the reactive gas to perform the TiO_2 etching. Another advantage is the much lower vapor pressure of $TiCl_4$ [35,36] compared to TiF_4, which reduces the chance of redeposition, which might lead to roughness and consequently scattering losses.

	SF_6	CHF_3	HBr	Cl_2	BCl_3
Resist	175	36	20	77	34
SiO_2	71	73	10	~0*	15
TiO_2	55	15	~0*	4	45

Table 2. Etch rates for different reactive gasses with a flow of 25 sccm
*no etching measured within measurement limit

First optimization steps are performed by starting with a 25 BCl_3 flow and adding Ar and O_2, as shown in figure 6a and b respectively. The etching rate increases slightly by adding Ar, which can be explained by the increased physical component of the etching. However the selectivity does not increase. When adding O_2, the etching rate of the resist increases drastically and the etch rate of TiO_2 and SiO_2 decreases, so adding O_2 to the etching process is not favorable. The influence of the HF power is shown in figure 6c, showing increased etching rates for higher HF powers. Increasing the HF power, increases the acceleration of the plasma, resulting in higher impact energy of the ions. The reduced selectivity towards resist, indicates that the resist is more sensitive to these higher impact energies than the TiO_2. 20 W is used as a minimum HF power, since lower powers are not stable. Figure 6d shows a decreasing etch rate, but higher selectivity for higher pressures. For lower pressures, the mean free path of the ions increases, causing less collisions of the ions when accelerated towards the substrate. As a result the impact energy will be higher, which again affects the resist more than the TiO_2. However, a lower pressure will result in a more directional plasma, which is required for straight sidewalls of the waveguide structure. Since a pressure of 5 mTorr still results in a selectivity higher than 1, this pressure is chosen to continue the process. Figure 6e shows the slightly increased etching rate of TiO_2 for increased BCl_3 flow, which is caused by the increased amount of ionized reactive gas. The selectivity is also slightly increased, since the EBL resist and the SiO_2 are not affected by the chemical component of the etching. At last HBr is added to the etching process. In Al_2O_3 processes BCl_3 is also used, but in combination with HBr [37], which makes the addition of HBr a promising step. As shown in figure 6e, the etch rates of TiO_2 and SiO_2 are hardly affected, but the etch rate of the EBL resist decreases drastically, resulting in a selectivity of about 2.7.
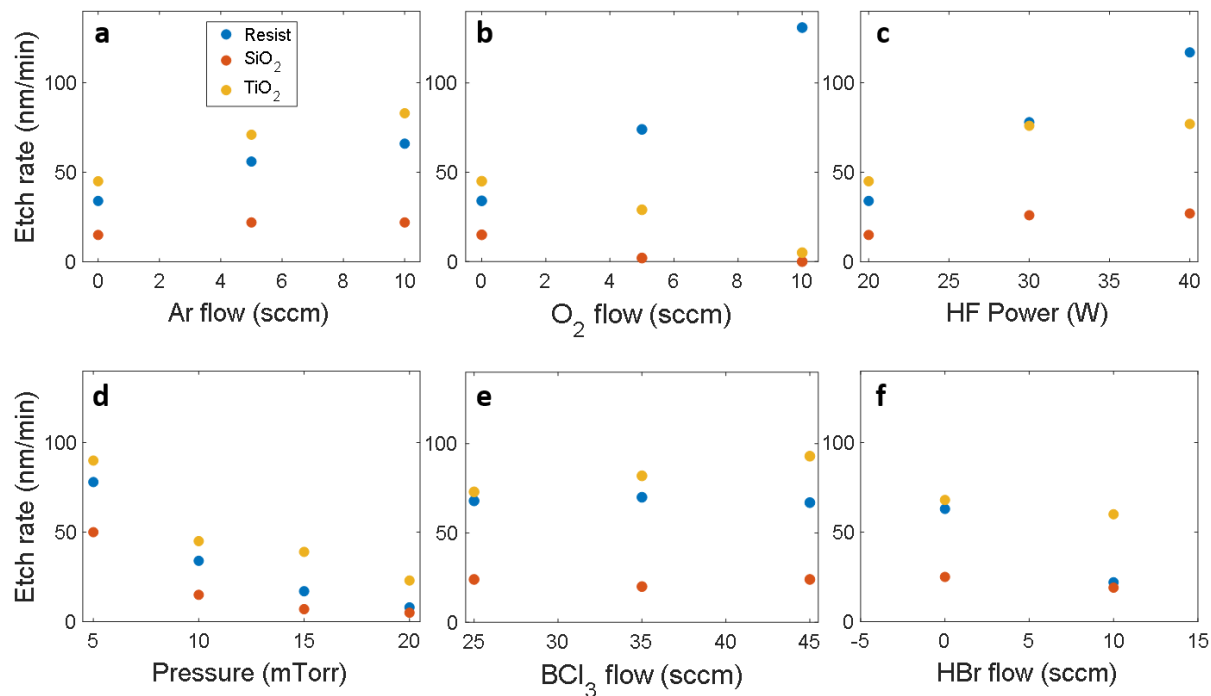
Figure 6. Etching rates of negative EBL resist, SiO_2 and TiO_2 for varying (a) Ar flow, (b) O_2 flow, (c) HF power and (d) pressure. Other settings during the etching process are as stated in table 1, except for the HF power in figure (c) and the pressure in figure (d).

For the final etching recipe that is used for waveguide fabrication, the following settings are used: pressure of 5 mTorr, HF power of 20 W, ICP power of 1500 W, temperature of 10 °C, a BCl_3 flow of 45 sccm and an HBr flow of 10 sccm. This recipe resulted in etching rates of the EBL resist, SiO_2 and TiO_2 of 29, 31 and 81 nm/min respectively, which shows a selectivity of TiO_2 towards the EBL resist of 2.8 and 2.6 towards SiO_2.

WAVEGUIDE FABRICATION

Two different waveguides are compared in terms of propagation losses. Waveguide A is fabricated prior to optimization of the fabrication process [33]. Waveguide B is fabricated after the optimization process. Waveguide A is fabricated using a TiO_2 layer deposited at a configuration similar to figure 1a. Patterning is performed using a photo contact lithography process, followed by a reactive ion etching step. Waveguide B is fabricated from a TiO_2 layer deposited at a point like the indicated point in figure 1b. The patterning is performed using EBL followed by an etching step using the optimized recipe.

Deposition

The TiO_2 film used for waveguide A is 140 nm thick and is deposited with an Ar flow of 35.4 sccm and an O_2 flow of 4.6 sccm. This corresponds to a deposition at a point similar to the indicated point in figure 1a. The other process parameters were a pressure of $6 \cdot 10^{-3}$ mbar, temperature between 20-30 °C, DC power of 500 W, 4" Ti target of 99.999% purity and a target to substrate distance of 176 mm. For waveguide B a 224 nm thick layer is deposited using an O_2 flow of 7.3 sccm and an Ar flow of 80 sccm is used, the other settings stayed the same. The substrate consists of a 4" Si wafer with an 8 μm thick thermal oxide layer.

Lithography

For waveguide A, photo contact lithography is performed using a 1.7 μm thick photoresist layer (Olin Oir 907.17), applied by spincoating using the standard recipe in the MESA+ cleanroom. Waveguide B is made using EBL. The spinning, exposure and development are performed as stated before in the E-beam lithography section. Waveguide A has a width of 1 μm and waveguide B has a width of 1.2 μm.

Etching

The etching for waveguide A is performed using an etching recipe based on SF_6 with the following settings, a pressure of 10 mTorr, temperature of 10 °C, ICP power of 1500 W, CCP power of 20 W, and SF_6, O_2 and Ar flow rates of 25, 6 and 5 sccm respectively. The etching of waveguide B is performed using an etching recipe based on BCl_3, as stated in before in the reactive ion etching section.

Cladding

Waveguide A is covered by a 1 μm thick SiO_2 cladding, which is deposited by e-beam evaporation from a 99,999% pure SiO_2 target in the BAK600 in the MESA+ cleanroom. The target to substrate distance is kept at 15 cm. Evaporation was chosen in order to keep the sample at room temperature to prevent crystallization of the TiO_2. The settings for the evaporations were a beam current of 200 mA and a base pressure of $6 \cdot 10^{-6}$ mbar.

Waveguide B is uncladded. Attempts were made to deposit the same cladding on top of waveguide B, as was used for waveguide A. In the case of waveguide B, the cladding cracked, making the device unsuitable for characterization. A measurement of this structure before applying the top cladding is used for comparison with waveguide A.

WAVEGUIDE CHARACTERIZATION

Light is coupled into the waveguides by fiber coupling, using a HeNe laser with a wavelength of 632.8 nm. A top view image is taken with a Point Grey monochrome camera (BFLY-U3-23S6M-C) to image the scattering losses. Figure 7 shows the images for waveguide A and B. A trace of the spiral is made to obtain the intensity as a function of the propagated distances, which is used to fit an exponential decay to the data, in order to obtain the propagation losses.
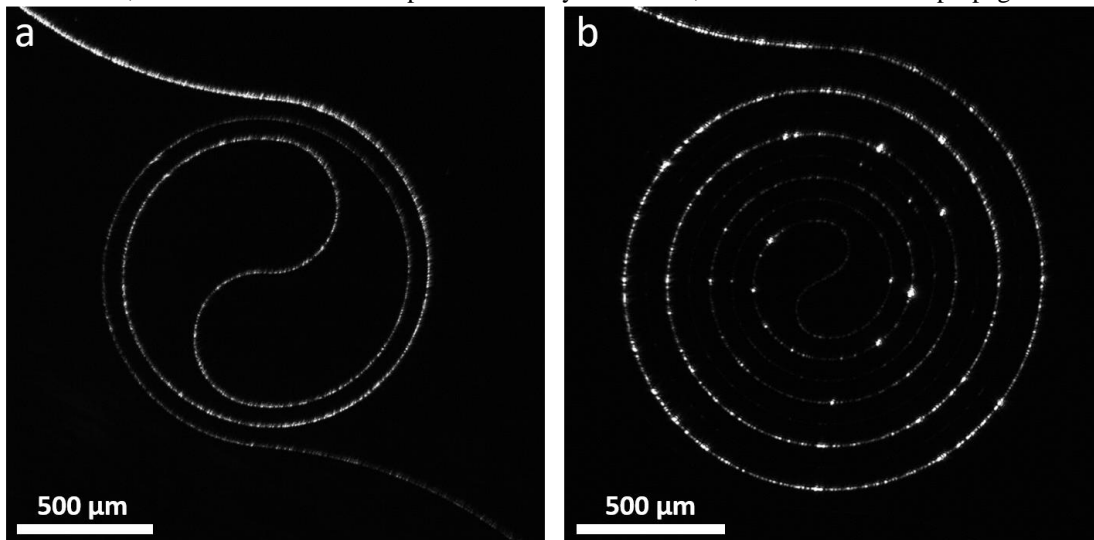
Figure 7. Topview image of the scattered light at a wavelength of 632.8 nm for (a) waveguide A and (b) waveguide B.

The resulting intensity trace and corresponding exponential fit are shown in figure 8. The calculated losses from the exponential fit for waveguide A are 7.84±0.72 dB/cm and for waveguide B 5.08±0.65 dB/cm. Where the error margin is obtained from the standard deviation of the fit parameters.
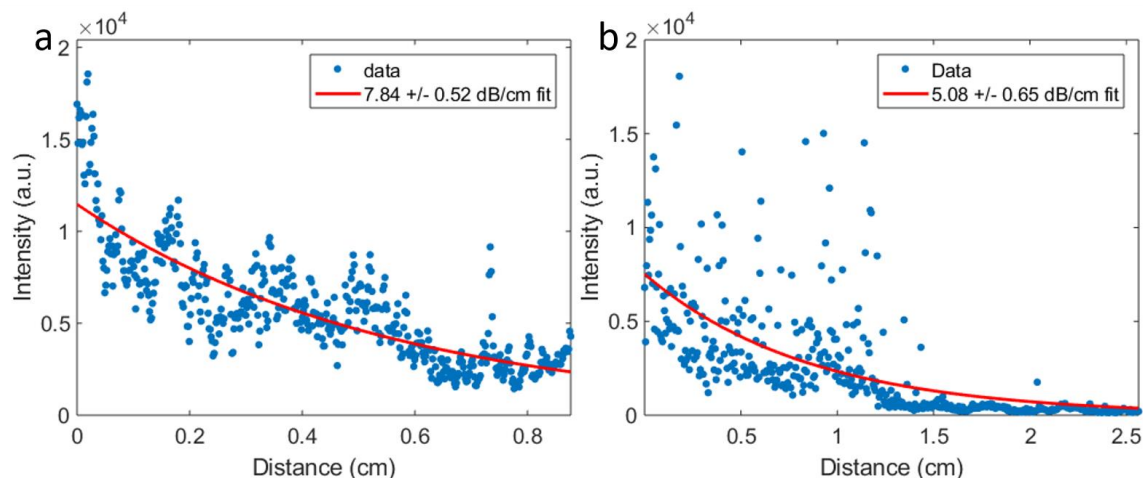
Figure 8. Exponential fit to the intensity profile of the scattered light of (a) waveguide A and (b) waveguide B, resulting in losses, at a wavelength of 632.8 nm. of 7.84 dB/cm and 5.08 dB/cm respectively.

Optimization of the deposition, lithography and etching processes resulted in, to our knowledge, the lowest propagation losses in TiO_2 channel waveguides compared to those shown in literature. Even lower losses can be expected after depositing an SiO_2 cladding, since this reduces the refractive index contrast between the core and cladding, which reduces the scattering losses due to surface and sidewall roughness.

CONCLUSION

The deposition, lithography and etching processes for the fabrication of TiO_2 channel waveguides were optimized. The DC reactive sputter deposition process was modified in order to take hysteresis out of the process. This was done by increasing the gas flow of Ar and O_2 into the reactor. The hysteresis free process allowed to deposit layers at a process configuration, that could not be reached in a process with hysteresis. This resulted in TiO_2 thin films with significantly lower propagation losses. An E-beam lithography process was developed using negative E-beam resist, in order to obtain resist patterns with high resolution, to reduce the sidewall roughness of the channel waveguide. The etching was performed by reactive ion etching. Different chemistries were compared, which showed BCl_3 to be the most beneficial for etching with high selectivity towards resist. The etch rate and selectivity was improved by increasing the BCl_3 flow and adding HBr to the process. This resulted in an etching recipe with a selectivity of 2.7 of TiO_2 towards the E-beam resist, where the etching using SF_6 showed a selectivity of approximately 0.2. Waveguides were fabricated with the process before and after optimization. The channel waveguide before optimization showed propagation losses of 7.84±0.52 dB/cm at a wavelength of 632.8 nm, after applying an SiO_2 top cladding by evaporation. The channel waveguide after optimization of all process steps showed losses of 5.08±0.65 dB/cm, also at a wavelength of 632.8 nm, without applying a top cladding. Lower losses are to be expected after covering the waveguide with an SiO_2 cladding.

REFERENCES

1.   M. Furuhashi, M. Fujiwara, T. Ohshiro, M. Tsutsui, K. Matsubara, M. Taniguchi, S. Takeuchi, and T. Kawai, "Development of microfabricated TiO_2 channel waveguides," AIP Adv. 1, 032102 (2011).

2.   J. D. B. Bradley, C. C. Evans, J. T. Choy, O. Reshef, P. B. Deotare, F. Parsy, K. C. Phillips, M. Lončar, and E. Mazur, "Submicrometer-wide amorphous and polycrystalline anatase TiO_2 waveguides for microphotonic devices," Opt. Express 20, 23821–23831 (2012).
3.   M. Landmann, E. Rauls, and W. G. Schmidt, "The electronic structure and optical response of rutile, anatase and brookite TiO 2," J. Phys. Condens. Matter 24, 195503 (2012).
4.   R. Ronchin, A. Chiasera, M. Montagna, R. Rolli, C. Tosello, and E. Al., "Erbium-activated silica-titania planar and channel waveguides prepared by rf-sputtering," in SPIE (2001), Vol. 4282, p. 38.
5.   T. Kornher, K. Xia, R. Kolesov, B. Villa, S. Lasse, C. S. Sandu, E. Wagner, S. Harada, G. Benvenuti, H. W. Becker, and J. Wrachtrup, "Amorphous Silicon-Doped Titania Films for on-Chip Photonics," ACS Photonics 4, 1101–1107 (2017).
6.   A. Bahtat, M. Bouderbala, M. Bahtat, M. Bouazaoui, J. Mugnier, and M. Druetta, "Structural characterisation of Er3+ doped sol–gel TiO_2 planar optical waveguides," Thin Solid Films 323, 59–62 (1998).
7.   A. Bahtat, M. Bouazaoui, M. Bahtat, C. Garapon, B. Jacquier, and J. Mugnier, "Up-conversion fluorescence spectroscopy in Er3+:TiO_2 planar waveguides prepared by a sol-gel process," J. Non. Cryst. Solids 202, 16–22 (1996).
8.   C. C. Evans, K. Shtyrkova, O. Reshef, M. Moebius, J. D. B. Bradley, S. Griesse-Nascimento, E. Ippen, and E. Mazur, "Multimode phase-matched third-harmonic generation in sub-micrometer-wide anatase TiO_2 waveguides," Opt. Express 23, 7832–7841 (2015).
9.   K. Hammani, L. Markey, M. Lamy, B. Kibler, J. Arocas, J. Fatome, A. Dereux, J.-C. Weeber, and C. Finot, "Octave Spanning Supercontinuum in Titanium Dioxide Waveguides," Appl. Sci. 8, 543 (2018).
10. C. C. Evans, K. Shtyrkova, J. D. B. Bradley, O. Reshef, E. Ippen, and E. Mazur, "Spectral broadening in anatase titanium dioxide waveguides at telecommunication and near-visible wavelengths," Opt. Express 21, 18582 (2013).
11. X. Guan, H. Hu, L. K. Oxenløwe, and L. H. Frandsen, "Compact titanium dioxide waveguides with high nonlinearity at telecommunication wavelengths," Opt. Express 26, 1055–1063 (2018).
12. O. Reshef, K. Shtyrkova, M. G. Moebius, S. Griesse-Nascimento, S. Spector, C. C. Evans, E. Ippen, and E. Mazur, "Polycrystalline anatase titanium dioxide microring resonators with negative thermo-optic coefficient," J. Opt. Soc. Am. B 32, 2288–2293 (2015).
13. L. He, Y. Guo, Z. Han, K. Wada, L. C. Kimerling, J. Michel, A. M. Agarwal, G. Li, and L. Zhang, "Broadband athermal waveguides and devices for datacom and telecom applications," in Proceedings of SPIE - The International Society for Optical Engineering (2018), Vol. 10537.
14. J. Bovington, R. Wu, K.-T. Cheng, and J. E. Bowers, "Thermal stress implications in athermal TiO_2 waveguides on a silicon substrate," Opt. Express 22, 661–666 (2014).
15. F. Qiu, A. M. Spring, and S. Yokoyama, "Athermal and high-Q hybrid TiO_2-Si_3N_4 ring resonator via an etching-free fabrication technique," ACS Photonics 2, 405–409 (2015).
16. B. Guha, J. Cardenas, and M. Lipson, "Athermal silicon microring resonators with titanium oxide cladding," Opt. Express 21, 26557–26563 (2013).
17. S. S. Djordjevic, J. Basak, B. Guan, K. Shang, H.-F. Liu, S. T. S. Cheung, L. Liao, and S. J. B. Yoo, "CMOS-compatible, athermal silicon ring modulators clad with titanium dioxide," Opt. Express 21, 13958 (2013).
18. A. Dhakal, A. Z. Subramanian, P. Wuytens, F. Peyskens, N. Le Thomas, and R. Baets, "Evanescent excitation and collection of spontaneous Raman spectra using silicon nitride nanophotonic waveguides," Opt. Lett. 39, 4025–4028 (2014).
19. C. C. Evans, C. Liu, and J. Suntivich, "TiO_2 Nanophotonic Sensors for Efficient Integrated Evanescent Raman Spectroscopy," ACS Photonics 3, 1662–1669 (2016).
20. C. C. Evans, C. Liu, and J. Suntivich, "Low-loss titanium dioxide waveguides and resonators using a dielectric lift-off fabrication process," Opt. Express 23, 11160–1169 (2015).
21. J. D. B. Bradley, C. C. Evans, F. Parsy, K. C. Phillips, R. Senaratne, E. Marti, and E. Mazur, "Low-loss TiO_2 planar waveguides for nanophotonic applications," in 2010 IEEE Photinic Society's 23rd Annual Meeting (IEEE, 2010), pp. 313–314.
22. L. Jiang, C. C. Evans, O. Reshef, and E. Mazur, "Optimizing anatase-TiO_2 deposition for low-loss planar waveguides," in Proc. of SPIE (2013).
23. M. Lamy, C. Finot, J. Fatome, J. Arocas, and J. C. Weeber, "Demonstration of High-Speed Optical Transmission at 2 µm in Titanium Dioxide Waveguides," Appl. Sci. 7, 631 (2017).
24. S. Berg and T. Nyberg, "Fundamental understanding and modeling of reactive sputtering processes," Thin Solid

Films 476, 215–230 (2005).

25. M. Hayrinen, M. Roussey, V. Gandhi, P. Stenberg, A. Saynatjoki, L. Karvonen, M. Kuittinen, and S. Honkanen, "Low-loss titanium dioxide strip waveguides fabricated by atomic layer deposition," J. Light. Technol. 32, 208–212 (2014).

26. K. R. Choi, J. C. Woo, Y. H. Joo, Y. S. Chun, and C. Il Kim, "The dry etching characteristics of TiO_2 thin films in N2/CF4/Ar plasma," Trans. Electr. Electron. Mater. 15, 32–36 (2014).

27. I. Hotovy, S. Hascik, M. Gregor, V. Rehacek, M. Predanocy, and A. Plecenik, "Dry etching characteristics of TiO_2 thin films using inductively coupled plasma for gas sensing," Vacuum 107, 20–22 (2014).

28. R. Adzhri, M. K. M. Arshad, M. F. M. Fathil, U. Hashim, A. R. Ruslinda, R. M. Ayub, S. C. B. Gopinath, C. H. Voon, K. L. Foo, M. N. M. Nuzaihan, A. H. Azman, and M. Zaki, "Reactive Ion etching of TiO_2 thin film: The impact of different gaseous," RSM 2015 - 2015 IEEE Reg. Symp. Micro Nano Electron. Proc. 1–4 (2015).

29. S. Norasetthekul, P. Y. Park, K. H. Baik, K. P. Lee, J. H. Shin, B. S. Jeong, V. Shishodia, E. S. Lambers, D. P. Norton, and S. J. Pearton, "Dry etch chemistries for TiO_2 thin films," Appl. Surf. Sci. 185, 27–33 (2001).

30. D. Kim, A. Efremov, H. Jang, S. Kang, S. J. Yun, and K.-H. Kwon, "Etching characteristics and mechanisms of TiO_2 thin films in HBr/Cl2/Ar inductively coupled plasma," Jpn. J. Appl. Phys. 51, (2012).

31. J. C. Woo, Y. S. Chun, Y. H. Joo, and C. I. Kim, "The dry etching property of TiO_2 thin films using metal-insulator-metal capacitor in inductively coupled plasma system," Vacuum 86, 2152–2157 (2012).

32. D. Depla, S. Heirwegh, S. Mahieu, J. Haemers, R. De Gryse, D. Depla, S. Heirwegh, S. Mahieu, J. Haemers, and R. De Gryse, "Understanding the discharge voltage behavior during reactive sputtering of oxides," J. Appl. Phys. 101, 013301 (2007).

33. I. Hegeman, M. Dijkstra, F. B. Segerink, W. Lee, and S. M. Garcia-Blanco, "Development of low-loss TiO2 waveguides," *Opt. Express*, in-press.

34. E. Särhammar, T. Nyberg, and S. Berg, "Applying "the upgraded Berg model" to predict hysteresis free reactive sputtering," Surf. Coatings Technol. 279, 34–38 (2015).

35. Titanium tetrachloride, ICSC No. 1230, International Labour Organization, https://www.ilo.org/dyn/icsc/showcard.display?p_card_id=1230&p_edit=&p_version=2&p_lang=en (accessed Jan. 13, 2020)

36. E. H. Hall, J. M. Blocher, and I. E. Campbell, "Vapor Pressure of Titanium Tetrafluoride," J. Electrochem. Soc. 105, 275–278 (1958).

37. J. D. B. Bradley, F. Ay, K. Wörhoff, and M. Pollnau, "Fabrication of low-loss channel waveguides in Al_2O_3 and Y_2O_3 layers by inductively coupled plasma reactive ion etching," Appl. Phys. B Lasers Opt. 89, 311–318 (2007).